Noname manuscript No.
(will be inserted by the editor)

Autonomous Mapping and Spectroscopic Analysis of Distributed Radiation Fields using Aerial Robots

Frank Mascarich · Mihir Kulkarni · Paolo De Petris · Taylor Wilson · Kostas Alexis

Received: date / Accepted: date

Abstract This paper presents a strategy for field estimation and informative path planning towards autonomous mapping and radiological characterization of distributed gamma radiation fields within confined GPS-denied environments using aerial robots. First, an online distributed radiation field estimation and spectroscopic analysis framework is presented which combines sequentially acquired measurements to estimate both the field intensity and gradient and propagate the belief over the initially unknown map, while simultaneously classifying each map region with respect to its dominating isotope. As such a process depends on the quality of the acquired measurements and given the limited endurance of small flying robots, we further contribute an informative path planner responsible for iteratively guiding the robot towards the next-best radiation measurement location such that high estimation confidence is achieved in short time. A divided global and local planning architecture is proposed enabling the robot to guide itself towards the radiologically most interesting areas quickly and acquire sufficient measurements within those. We further develop a tailor-made collision-tolerant micro flying robot that is equipped with a lightweight scintillator and silicon photomultiplier combination, alongside GPS-denied localization and mapping capabilities. A set of experimental studies are presented involving the autonomous characterization of distributed radiation fields containing live uranium ore and radium sources within GPS-denied industrial settings.

Keywords Radiation Mapping · Path Planning · Aerial Robots

F. Mascarich
University of Nevada, Reno
E-mail: fmascarich@nevada.unr.edu

M. Kulkarni
University of Nevada, Reno
Norwegian University of Science and Technology
E-mail: mkulkarni@nevada.unr.edu

P. De Petris
Norwegian University of Science and Technology
E-mail: paolo.de.petris@ntnu.no

T. Wilson
University of Nevada, Reno
E-mail: trwilson@unr.edu

K. Alexis
Norwegian University of Science and Technology
E-mail: konstantinos.alexis@ntnu.no

1 Introduction

In this work, autonomous robotic technologies are developed in order to facilitate the monitoring and characterization of nuclear sites. A history of research, development and utilization of nuclear technology, alongside the natural occurrence of radioactive materials calls for the need to develop new and advanced means to autonomously survey, map and characterize complex and distributed gamma radiation fields. Nuclear technology is used in a multitude of applications including—but not limited to—nuclear power generation, nuclear weapons, medical applications (e.g., medical radiography), industrial use (e.g., industrial radiography), commercial applications (e.g., smoke detectors), and food processing (e.g., insect control). The effect is that the world is now host to a complex set of facilities that require careful monitoring and maintenance. Considering the effect of nuclear waste alone, it is estimated that more than a quarter million metric tons of highly radioactive waste is deposited in storage facilities near nuclear power plants and weapons production facilities worldwide. The U.S. accounts for over $90,000$ metric tons of nuclear waste alone [19]. Such nuclear waste is stored in complex facilities, either in near-surface disposal at ground level or in caverns below ground level (at depths of tens of meters), or deep geological

disposal at depths between 250 – 1000 m for mined repositories or 200 – 50000 m for boreholes [39]. Similarly, the importance of automated and robotized radiation characterization is further emphasized by looking at the number of nuclear reactors closed across the world [38] (with more to close soon) as shown in Figure 1. These are all examples of complex nuclear facilities for which robotic systems capable of delivering comprehensive monitoring and surveying would have a major impact and improve our ability to reduce risks of contamination, respond to possibly catastrophic nuclear accidents, and characterize settings presenting natural or artificially introduced radioactive materials.

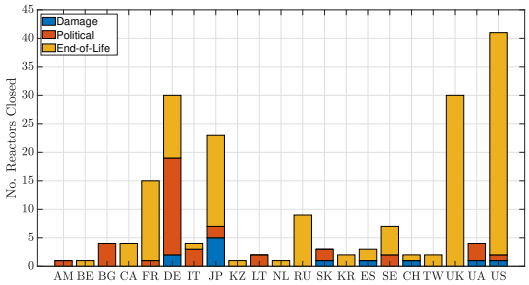

Fig. 1 An indicative application of robotized radiation characterization is to perform inspections in decomissioned nuclear power plants. Across the world, a set of reactors are already closed and more are to be decommissioned soon. The figure presents the number of reactors closed for the following reasons: following damage in an accident or serious incident, prematurely by political decision or consideration, or having fulfilled their purpose and being no longer economic to run across 21 countries, namely: Armenia (AM), Belgium (BE), Bulgaria (BG), Canada (CA), France (FR), Germany (DE), Italy (IT), Japan (JP), Kazakhstan (KZ), Lithuania (LT), the Netherlands (NL), Russia (RU), Slovakia (SK), South Korea (KR), Spain (ES), Sweden (SE), Switzerland (CH), Taiwan (TW), United Kingdom (UK), Ukraine (UA), and USA (US).

In the literature, multiple efforts of the research community can be identified with the majority relating to the teleoperated use of ground robots [4, 13, 20] including specialized crawlers that entered the reactor buildings of the Fukushima Daiichi Nuclear Power Station [32] or are capable of characterizing miles of contaminated pipes installed in enrichment facilities [15], deployment of unmanned aerial vehicles in open-ended environments [4, 34], underwater robots for pipe inspection [25] and more. Despite the significant efforts and the pioneering contributions of the community, autonomous mapping and characterization of distributed nuclear radiation fields especially within complex facilities is far from achieved. Iconic examples of environments of interest include the "sarcophagus" of Chernobyl's Unit 4, the reactors of the Fukushima Daiichi nuclear power plant requiring continuous inspection for years to come, the Plutonium Uranium Extraction Plant (PUREX) tunnels at the Hanford site, the McArthur River mine in Canada representing the world's largest uranium producing mine, and a collection of other facilities and buildings of larger or smaller scale.

Motivated by the importance of automating radiological surveys of key infrastructure and aiming to enable seamless robotic deployments, in this work we present a new method and a prototype system realization for autonomous surveying, mapping, and distributed gamma radiation field estimation inside confined and possibly GPS-denied settings using aerial robots. The method departs from prior works on single- or individual-source localization, or contributions in 2D/3D field intensity estimation, and provides a fully 3D strategy for the estimation of intensity, gradient, and spectroscopic properties of complex distributed gamma radiation fields, alongside a next-best-radiation-measurement path planning algorithm capable of commanding the aerial robot so that the estimation of the gamma radiation field is achieved efficiently within complex facilities.

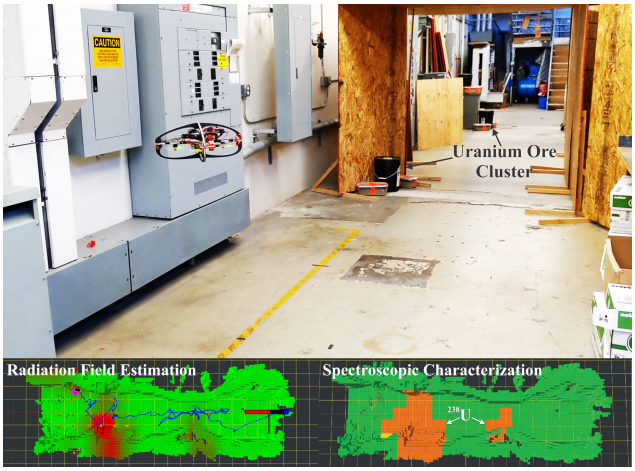

Fig. 2 An instance of the prototype RMF-γ aerial robot performing an autonomous radiological surveying mission inside a GPS-denied environment based on the proposed radiation field mapping and informative path planning method.

In particular, the proposed strategy first contributes an iterative distributed gamma radiation field mapping and spectroscopic analysis technique that combines a field estimation step based on the measurements gathered so far, followed by a field propagation step, with a classification scheme identifying which isotope dominates every subset of the map. To enable reliable distributed gamma field estimation, the method introduces a metric based on spatial entropy to characterize the level of confidence attributed to the estimated field intensity and gradient at any map location. As the quality of the field mapping depends upon the quality of the radiological measurements acquired by the robot, we further contribute an informative path planner that is responsible for guiding the flying robot through a sequence of points and collision-free paths that at any instance maximize the likelihood to map the—generally distributed—radiologically ac-

tive areas of the map. To achieve this task in a manner that respects the limited endurance of small flying robots, the planner classifies the different areas of the map with respect to how confident the robot is regarding the quality and spatial distribution of the data sampled in each region. Importantly, the overall strategy runs onboard a tailor-made flying robot called the Resilient Micro Flyer-gamma (RMF-γ). RMF-γ is a micro-sized aerial robot capable of autonomous GPS-denied navigation that further integrates a Thallium-activated Cesium Iodide CsI(Tl) scintillator combined with a silicon photomultipler in order to acquire gamma radiation measurements, enabling field intensity estimation and spectroscopy. The radiation measurements are associated with the real-time estimates of the robot's trajectory to effectively deliver, in real-time, 3D maps that are annotated with the estimated radiation intensity, gradient, and dominating radioisotope in each region. Figure 2 presents an instance of the robot conducting one such autonomous radiological survey in a GPS-denied and confined environment.

Towards a thorough evaluation of the proposed approach and prototype system realization, a set of studies were conducted using the developed RMF-γ aerial robot deployed in realistic environments containing real nuclear radiation sources such as uranium ore and radium. As demonstrated, the contributed strategy delivers reliable and efficient autonomous radiation field estimation and spectroscopic characterization using micro-sized flying robots with constrained endurance operating inside complex, GPS-denied and confined environments.

The remainder of this paper is organized as follows. Section 2 outlines related work, followed by the description of the developed RMF-γ robot and the properties of the associated system's radiation measurement, mapping, and surveying capabilities in Section 3. Subsequently, Section 4 presents the proposed radiation mapping and spectroscopic analysis method, while Section 5 details the contributed informative path planner for radiation field characterization. Evaluations are presented in Section 6, followed by conclusions in Section 7.

2 Related Work

A multitude of research efforts have considered the problem of radiation field characterization, with a subset of them specifically considering the case of nuclear sources [2, 3, 5, 14, 36]. Notably, the majority of published work in the domain has focused on the detection and estimation of discrete sources. Relevant examples include contributions on source localization through maximum likelihood estimation [2, 5], numerical adjoints combined with Bayesian formulations [14] and those based on particle filter estimation [36]. At the same time, an extensive literature is available on the general problem of distributed field estimation that primarily focuses on non-nuclear sources and utilizes either networks of wireless sensors [21, 37] or mobile robots [18]. Similarly, the community has examined the problem of active source localization, whereas "active source" implies radiological, chemical and other types [24, 30, 40]. Nuclearized robotics research [4, 6, 12, 20, 27, 28, 31, 34, 35] has grown to be an important subdomain and several contributions have been proposed. The authors in [31] present a method for adaptive source seeking through successive-elimination. The paper in [6] details an approach on distributed guidance by means of information gradients to estimate the radiation distribution tested using a "radiation analog" source. The authors in [27, 28] handle multiple sources but only evaluate their methods in simulation. Aiming to better inform the information gathering paths of a ground robotic system, the authors in [4] employ scene segmentation based on aerial views. Focusing on large-scale environments, the work in [35] uses a helicopter UAV to map radiation over large environments. Tailored to post–disaster radiation mapping, the contribution in [34] presents a grid-based Bayesian estimator for single source localization and contour analysis for multiple sources.

Considering a different aspect of the problem, the work in [12] incorporates radiation sensing in order to enable a robot to navigate an environment with ionizing radiation, while avoiding areas of high field intensity in order to ensure its safety. Exploiting new compact Compton camera technologies, the authors in [32] present a system for radiation imaging using a crawler robot inside the reactor buildings of the Fukushima Daiichi nuclear power station. In an analogous manner, the work in [1] demonstrates the use of a Compton event camera onboard a micro aerial vehicle for the purposes of gamma radiation source localization. Employing a team of small aerial robots, the contribution in [33] presents a method for the localization of ionizing radiation sources using onboard pixel detectors, while the work in [16] details plug-and-play radiation sensor components for unmanned aerial vehicles. Emphasizing field demonstration, the authors in [11] present a heterogeneous robotic system capable of performing radiation surveys.

In addition to this body of research, our prior work in the domain has contributed three distinct capabilities, namely a) single-source localization with an aerial robot [8] using a single detector and dwelling at each measurement location, b) distributed radiation field estimation in 2D using ground robots with a specialized detection apparatus involving three scintillators [23], and c) distributed 3D radiation field estimation using a micro aerial vehicle equipped with a scintillator [22]. As compared to these works, this paper contributes five significant advances. First, the presented method makes no assumptions with respect to the source strength or its distribution within the environment and can map complex 3D radiation fields. This contribution highlights the real-

world applicability of the method and its ability to map distributed radiation sources. Such distributed sources may be made of a variety of isotopes placed closely together such that there does not exist a span of background radiation intensities between them. Second, the method requires only a single, low-cost radiation sensor, and like [22] does not require an explicit "dwelling" behavior. "Dwelling", in this context, refers to commanding the platform to remain at a given position for a given amount of time in order to reduce measurement uncertainty of radiation field intensity at a particular point. Third, the field mapping strategy is not limited to intensity and gradient estimation but also performs spectroscopic analysis and thus characterizes every region of the radiation field with respect to its dominant isotope. Fourth, the presented novel planning algorithm iteratively guides the robot to the next-best-radiation-measurement location both from a local and a global standpoint. The presented planning algorithm allows the radiological mapping of confined and complex environments in 3D, thereby rendering it applicable to real-world contaminated environments. Fifth, the method is deployed and experimentally verified using a custom-made micro-sized and collision-tolerant aerial robot enabling the seamless operation in confined environments not limited by any terrain.

3 The RMF-γ Aerial Robot for Radiation Surveying

This section presents the developed robotic system for distributed radiation field surveying and characterization, and focuses on the integrated gamma radiation detector and the associated measurement principles.

3.1 The RMF-γ aerial robot for radiation surveying

The design of the RMF-γ aerial robot—its first version presented in [22], and presented in Figure 3—is tailored to the need of autonomous estimation of distributed gamma radiation fields in GPS-denied and confined environments. The RMF-γ quadcopter features a carbon-balsa sandwich frame, an mRo X2.1 Rev. 2 autopilot running the Ardupilot firmware, as well as a Realsense T265 stereo visual-inertial system and a Realsense D435i RGB-Depth sensor interfaced with a Khadas VIM3 Pro single board computer (SBC). The SBC is also responsible for running all the 3D occupancy mapping, distributed gamma radiation field estimation, spectroscopy, and informative path planning for autonomous surveying in GPS-denied and confined environments. The total weight of the system including its battery is 639 g.

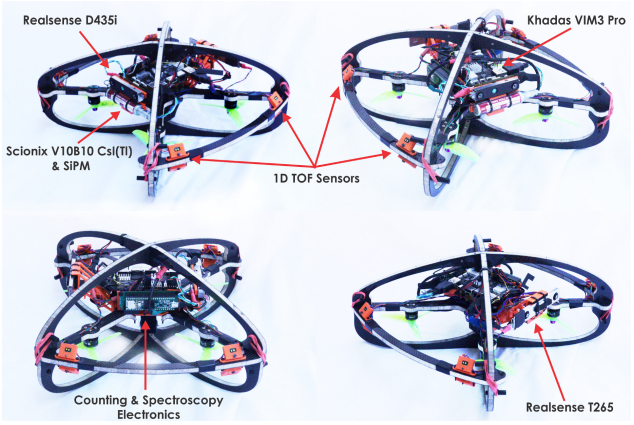

Fig. 3 RMF-γ views and main electronic components.

3.2 Radiation Sensing

In this section we detail both the sensing and processing components alongside the underlying measurement principles that facilitate gamma radiation detection onboard the RMF-γ aerial robot.

3.2.1 Onboard Radiation Detection

The selection of radiation detection principle and specific device was driven by the need for a) high sensitivity, b) low weight and power consumption, alongside c) spectroscopic resolution. Optimizing for these criteria, we integrated a Scionix V10B10 Thallium-activated Cesium Iodide CsI(Tl) scintillator combined with a Silicon Photomultipler (SiPM) and associated counting and spectroscopy electronics (depicted in Figure 4) with a total weight of 41 g. In further detail, the radiation detector consists of a) the Scionix V10B10 CsI(Tl) scintillation crystal, b) a small SiPM, and c) a custom-designed pulse counting and spectroscopy circuit that weighs only 23 g. The Scionix detector is a cylindrical package (66 mm long, 16 mm wide) which provides analog voltage pulses that correspond to incident gamma photons colliding with the scintillation crystal. The amplitude of each pulse is proportional to the energy released by the corresponding gamma photon. Different isotopes emit gamma photons with a unique set of energies which allows spectroscopic analysis. Therefore, to implement spectroscopy, the processing electronics must not only count the number of pulses present on the scintillator's output, but also log the amplitude of these pulses. Accordingly, our custom-built scintillator processing electronics consists of a series of 32 comparators comparing reference voltages that are generated by a resistor ladder against the output signal from the scintillator's preamplifier. The outputs of the comparators are read by a 32-bit, 180 MHz ARM microcontroller and the system can discern between 32 different pulse amplitudes, therefore offering low resolution spectroscopy and separate counting of

gamma radiation at different energy levels. Updated measurements are reported by the microcontroller at 10 Hz.

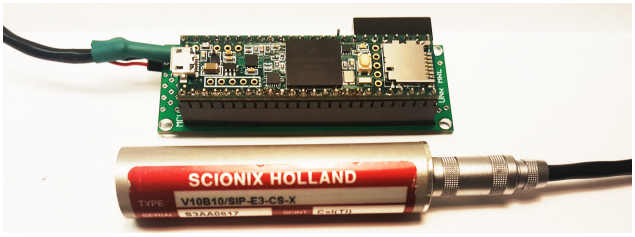

Fig. 4 The Scionix V10B10 Thallium-activated Cesium Iodide CsI(Tl) scintillator combined with a Silicon Photomultipler (SiPM) and interfaced by our custom-built counting and spectroscopy electronics.

3.2.2 Radiation Counts

The previously described radiation detector that is integrated onboard the RMF-γ is used to detect high-energy particles emitted by radioactive materials. In particular, the gamma radiation intensity is evaluated by measuring radiation counts received by the detector which in turn may be modeled as a composition of the signal from radiation sources and the effect of the natural background radiation [9, 17].

Given a distributed radiation field of intensity $\mathcal{S}(\mathcal{M})$ over the environment map $\mathcal{M}$, and assuming that the effect of the distributed radiation field can be modelled as the additive effect of N_s small point sources s^i, $i = 1,...,N_s$, then the mean radiation Counts Per Second (CPS), denoted as y, received at a position $\mathbf{p}_\kappa$ takes the form [10, 17]:

$$E(y_{\mathcal{S}}^{\mathbf{p}_\kappa}) = \sum_{i=1}^{N_s} \frac{Aev_{s^i}}{4\pi||\mathbf{p}_\kappa - \mathbf{p}_{s^i}||^2}, \tag{1}$$

where A and e are the area and the efficiency of the detector, v_{s^i} is the s^i source intensity, and $||\mathbf{p}_\kappa - \mathbf{p}_{s^i}||^2$ denotes the Euclidean distance from the detector to the source s^i located at $\mathbf{p}_{s^i}$. Given that the detector is set to sample data at a fixed rate F_d and considering the general case that during the time interval between the $\kappa-1$ to κ sample $T_d = 1/F_d$ (1 sample) the robot is moving along some curve $\mathcal{C}_{\kappa-1}^{\kappa}$, then the resulting radiation CPS measurement, denoted as Y, reported at time κ, with the robot arriving at position $\mathbf{p}_\kappa$, $E(Y^{\mathbf{p}_\kappa})$ takes the form:

$$E(Y_{\mathcal{S}}^{\mathbf{p}_\kappa}) = \int_{\mathcal{C}_{\kappa-1}^{\kappa}} \sum_{i=1}^{N_s} \frac{Aev_{s^i}}{4\pi||\mathbf{p}_\kappa(\mathbf{r}) - \mathbf{p}_{s^i}||^2} d\boldsymbol{\sigma} = \int_{\kappa-1}^{\kappa} \sum_{i=1}^{N_s} \frac{Aev_{s^i}}{4\pi||\mathbf{p}_\kappa(\mathbf{r}(t)) - \mathbf{p}_{s^i}||^2} |\mathbf{r}'(t)|dt, \tag{2}$$

where $\mathbf{r}$ is a parameterization of the curve $\mathcal{C}_{\kappa-1}^{\kappa}$ such that the values it takes at $\kappa-1$ and κ are the extremes of $\mathcal{C}_{\kappa-1}^{\kappa}$. At the same time, the detector also receives radiation from the natural background (also following the Poisson distribution) that takes the form:

$$E(Y_b^{\mathbf{p}_\kappa}) = T_d Aev_b, \tag{3}$$

where v_b is the background intensity. Since the signal due to the distributed radiation field $\mathcal{S}(\mathcal{M})$ and background are independent, the total radiation count continues to follow the Poisson distribution and the expected value ζ_κ reported at time κ takes the form:

$$\zeta_\kappa = E(Y^{\mathbf{p}_\kappa}) = E(Y_{\mathcal{S}}^{\mathbf{p}_\kappa} + Y_b^{\mathbf{p}_\kappa}) = T_d Aev_b + \int_{\kappa-1}^{\kappa} \sum_{i=1}^{N_s} \frac{Aev_{s^i}}{4\pi||\mathbf{p}_\kappa(\mathbf{r}(t)) - \mathbf{p}_{s^i}||^2} |\mathbf{r}'(t)|dt. \tag{4}$$

The quantities A and e of Eq. (4) are determined by the calibration of the detector in a pre-characterized chamber. The signal intensities v_{s^i} are determined by the distributed radioactive source field which is initially unknown. The background intensity rate v_b can be derived through preliminary measurements away from the expected radiation field (exploiting the fast decay of the inverse square law).

3.2.3 Spectral Readings

The aforementioned radiation detection module is also equipped with spectroscopy capabilities, allowing it not only to count instances of gamma rays impacting the detector crystal, but also to measure their energy. Any source of gamma radiation emits rays at a particular set of energies which are related to the specific decay process for that isotope. For example, ^{137}Cs emits gamma radiation at primarily 662 keV. This energy level will be reflected as the amplitude of the voltage pulse emanating from the scintillator's pre-amplifier. Using the comparator array that is described in Section 3.2.1, this pulse height will result in all comparators between the comparator connected to the lowest reference voltage and comparator connected to the reference voltage immediately below the incoming pulse voltage, changing the state of their output. The microcontroller maintains an array of 32 integers and upon the receipt of an interrupt signal indicating this state change, increments the value of the array at the index corresponding to the comparator that was triggered. At a rate of 10 Hz, the microcontroller calculates and reports the detected spectrum of channel counts, $\mathbf{Q}^\kappa$. Given the counting array described above and denoted by $\mathbf{G}^\kappa$, the correct spectral count for each channel is calculated by the following:

$$\mathbf{Q}_i^\kappa = \mathbf{G}_i^\kappa - \mathbf{G}_{i+1}^\kappa, i \in [0,31], \quad \mathbf{Q}^\kappa = \{\mathbf{Q}_i^\kappa\}, \forall\, i = \{0...31\}, \tag{5}$$

where $\mathbf{G}_i^\kappa$ is the originally obtained value from the counting array at time κ in channel i, and $\mathbf{Q}_i^\kappa$ is the resulting number of pulses detected in channel i at time κ.

3.2.4 Detector Calibration

The onboard integrated Scionix V10B10 is a miniaturized Thallium-activated Cesium Iodide CsI(Tl) SiPM scintillation detector integrating a Silicon Photomultiplier and having built-in temperature compensated bias generator and a preamplifer. Its voltage output consists of pulses with a width of 2.2 μs and an amplitude that is proportional to the energy of the gamma photon that triggered the pulse. The frequency of the pulses, generally reported in Counts Per Second, is proportional to the gamma ray field intensity incident upon the detector. It is noted that various factors such as the size of the crystal, the shielding from the scintillator's enclosure, and properties of the SiPM determine what proportion of gamma emissions a scintillator will detect.

Calibration of such a scintillator consists of four components: a linearity evaluation, an orientation evaluation, a count calibration, and an energy calibration. The first three components utilize a calibration chamber which contains a radioactive source of known activity. The chamber utilized in this work contains a ^{137}Cs source with an activity of 6.66 MBq. However, due to various complex factors such as the shape of the calibration chamber, the materials from which it is constructed, and the various windows and attenuation surfaces between the source and the chamber, the characteristic used for calibration is the dose rate. Using the time since the last chamber calibration, the present-day dose rate at various distances can be calculated using the half-life of ^{137}Cs.

The first step, a linearity evaluation, is used to evaluate the count rate response of the detector and its interfacing electronics when exposed to sources of increasing intensity. First, due to the design of the electronics and of the scintillator itself, at some radiation intensity, the detector's output will be saturated. This intensity level was not found after exposing the detector to dose rates as high as 10 mRem/hr, which greatly exceeds the anticipated radiation exposure levels. Second, we expose the scintillator to a field of known intensity at various distances from the source to confirm that the scintillator has a dose rate response in agreement with the inverse square law of radiation propagation. These results are shown in subplots (a) and (b) of Figure 5.

The second step of the calibration process, an orientation evaluation, is necessary given that the detector will be used on a mobile platform, in an unknown environment. This process concerns determining the directionality of the scintillator in response to its shape and the position of the integrated electronics. For the purposes of this calibration, we define the roll axis of the scintillator to be the cylindrical axis of the detector, the pitch axis to be parallel to the line connecting the interface pins on the rear of the detector, and the yaw axis to be perpendicular to the roll and pitch axes. The scintillator is placed at a single distance from the source in the calibration chamber, and is rotated around its yaw axis. Variation around its roll and pitch angles is not required due to the symmetrical nature of the scintillation crystal. The results of this calibration procedure on our scintillator are shown in subplot (c) of Figure 5. As shown, the scintillator has a mostly symmetric response with an approximate 50% decrease in detected counts over a small arc of orientations when its back faces the source (due to the interfacing electronics inducing a shielding effect). This step yields the fact that the detector has a narrow cone of reduced sensitivity to sources located directly behind the crystal.

The third step of the calibration process, the count calibration, is to determine the scintillator's efficiency. For accurate radiation field estimation, it is necessary to determine the relationship between a scintillator's count rate, and the true dose rate of the field. This step takes place by collecting data from the lowest channel of the counting circuit. Due to the design of the counting circuit, this channel is the sum of pulses counted at its reference and all channels above it, and is therefore a measure of all counts on all channels. The scintillator is fixed in one position and oriented in an ideal direction, directly facing the source. The detector is exposed to three field intensity levels, 0.1 mRem/hr, 1 mRem/hr, and 10 mRem/hr. This allows for the calculation of the linear relationship between the measured Counts Per Second and the dose rate as presented in subplot (a) of Figure 5.

The final step of a scintillator calibration determines the energy response of the scintillator when exposed to different radioactive sources. While sources of a particular isotope produce pulses of varying amplitude due to back-scattering and other effects, a set of dominant amplitudes are produced, characteristic to the exposed isotope. Figure 6 shows results of this calibration for ^{137}Cs, ^{60}Co, ^{238}U, ^{226}Ra, ^{232}Th, and ^{22}Na.

3.2.5 Sources of Error and Noise

For any given radiation detector, a number of reasons can lead to fluctuation in the response. Those include—but are not limited to—the following a) possible drift of the operating characteristics, b) sources of random noise within the interfacing electronics, c) dead times due to the time required to separate two interaction events, and d) statistical noise arising from the discrete nature of the measured signal (which follows the Poisson distribution) [17]. Among those, the latter is typically the most significant and represents an irreducible minimum amount of fluctuation that will necessarily be present in the detector output signal despite the quality of the scintillator and interfacing circuitry. This arises from the fact that the charge generated within the detector by a quantum of radiation is not a continuous variable but rather represents a discrete number of charge

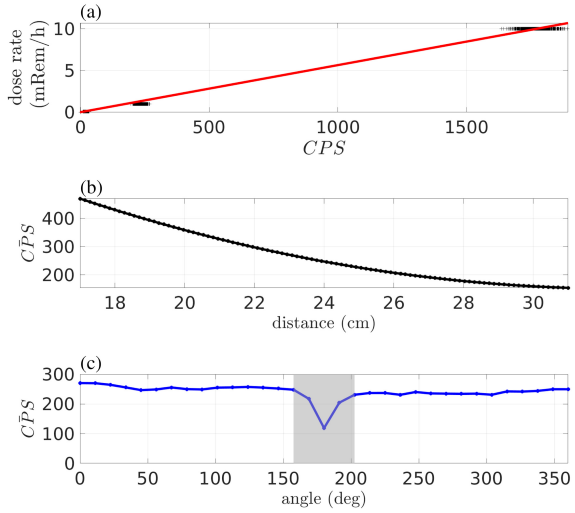

Fig. 5 Subplot (a) depicts the identified linear relation (red line) between the utilized scintillator measured in Counts Per Second (CPS) and the field dose rate, measured in mRem/hr. The scintillator is placed in a calibration chamber with its head directly facing the source. The data gathered (black '+') allows to relate the measured CPS to the actual field dose rate which is essential for radiological characterization. Subplot (b) shows the calibration of average CPS value ($C\bar{P}S$) to distance by placing the scintillator at distances of 19 cm to 31 cm from the source. The scintillator is positioned inside the calibration chamber with its head facing the source. The data presented complies with the inverse square law. Subplot (c) depicts the calibration of the average CPS value against various orientations of the scintillator as compared to the source. As shown the scintillator is largely symmetric with the exception of a small narrow cone of reduced sensitivity which appears when the scintillator faces exactly away from the source.

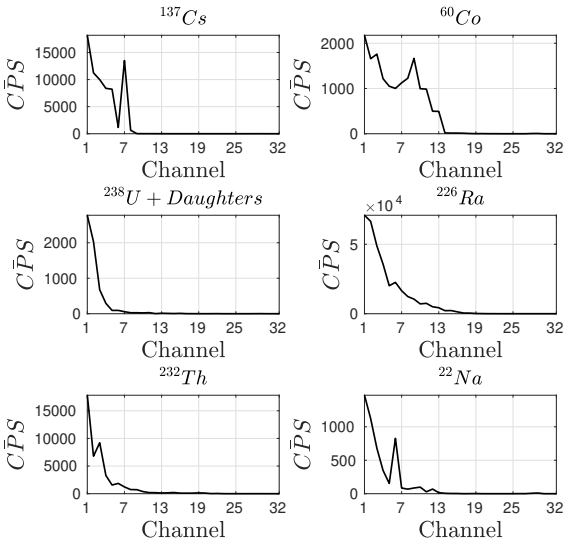

Fig. 6 Plot showing the results of the energy calibration in which the scintillator's energy response to different gamma sources was evaluated. Specifically, the cases for ^{137}Cs, ^{60}Co, ^{238}U, ^{226}Ra, ^{232}Th, and ^{22}Na are shown and the different characteristic energy results per channel are presented.

carriers. The Poisson distribution models this effect, and for a mean value λ, the variance is λ and the standard deviation $\sqrt{\lambda}$. For multiple measurements acquired at a certain point, the Poisson distribution can be approximated by a Gaussian distribution.

The issue of spectral noise is significantly different. While a particular isotope will emit gamma radiation at a particular energy level, the resulting spectra covers a large number of channels measured by the detector circuit. For example, referring to Figure 6, the ^{137}Cs plot clearly shows its characteristic peak at 0.6617 MeV in channel 7, as well as a significant number of counts in lower channels. This noise is mainly due to two factors: Compton scattering and background noise. Compton scattering is the effect of a particle collision occurring before being detected by the scintillator which results in a loss of some proportion of the original emission's energy, while the noise from background sources of radiation, especially in the presence of weak sources, also contributes additional noise to the resulting spectra. Fortunately, the characterization approach presented in this work does not rely on a precise energy calibration or peak channel detection at the level of each individual channel but rather exploits the relative response captured in each channel against the remaining channels, and thus is robust to such sources of noise.

3.3 Environment Mapping and Representation

To enable the association of the estimated radiation field with the environment within which a survey takes place, and to offer the necessary representation for autonomous path planning, RMF-γ fuses the onboard Realsense T265 and D435i sensor data. The Realsense T265 sensor offers highly compact visual-inertial odometry estimation—and when desired, loop closure capabilities—with a power-efficient ASIC implementation. The Realsense D435i sensor provides point-clouds with a maximum range of 3 m and a field of view equal to $87^\circ \times 58^\circ$. The odometry updates—and associated pose transformations—provided by the T265 stereo visual-inertial system are associated with the RGB-Depth point-clouds of the D435i thus allowing to reconstruct a dense pointcloud of the explored environment and also populate a 3D occupancy map based on Voxblox [29]. Voxblox utilizes voxel hashing for fast lookups of voxel information from its 3D coordinate and allows for incrementally constructing the Euclidean Signed Distance Field (ESDF) maps from the Truncated Signed Distance Field (TSDF) maps, and occupancy maps.

3.4 Autonomous Radiological Surveying

In the subsequent sections, the overall algorithmic approach that enables the autonomous distributed radiation field characterization based on the RMF-γ aerial robot equipped with a CsI(Tl) SiPM gamma radiation detector is presented. In particular, Sections 4 & 5 present the two core functionality modules of a) real-time distributed radiation field estimation ("rad-mapping") given onboard radiation measurements without the need for dwelling, and b) the uncertainty-aware curiosity-driven informative path planning that is responsible for planning paths towards the measurement locations that allow the fast and high-fidelity estimation of the gamma radiation field ("rad-sniffing"). The solution exploits the localization and mapping capabilities onboard the aerial robot, enabling it to reconstruct detailed 3D and occupancy maps, alongside estimating its pose, in GPS-denied environments. A block diagram of the key functionalities onboard RMF-γ is depicted in Figure 7.

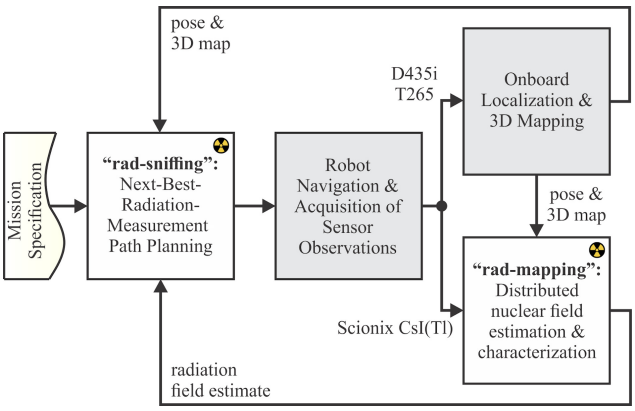

Fig. 7 Overall block diagram depicting the core functional elements running onboard the prototype RMF-γ aerial robot capable of autonomous radiological surveying in GPS-denied and confined environments.

4 Distributed Radiation Field Characterization

The presented work addresses the problem of autonomous distributed 3D radiation field estimation and spectroscopic characterization proposing both an algorithm for field estimation given a set of sequentially collected measurements, and an informative path planner responsible for selecting the next-best radiation measurement point for a robot to go in order to best support the field mapping process in deriving a high-quality and high-confidence result in a short period of time. The underlying motivational scenario is that a small aerial robot enters a large-scale but GPS-denied and geometrically confined environment within which it performs accurate radiation mapping and spectroscopic analysis. In this section we present the radiation mapping and spectral characterization algorithm. Figure 8 presents the mapping strategy from a high level perspective.

Problem Definition Let the robot configuration at time t_κ be the flat state $\boldsymbol{\xi}_\kappa = [\mathbf{p}_\kappa | \psi_\kappa]$ that combines the vehicle's position $\mathbf{p}_\kappa = [x_\kappa, y_\kappa, z_\kappa]$ and heading ψ_κ. The problem of distributed gamma radiation field estimation and spectroscopic characterization, as considered in this work, is that of identifying the intensity, dominant isotope, and locations of a large number of point sources, with each of them obeying the inverse square law for their intensity and a Poisson model for the noise of each measurement.

To enable addressing this problem, the method makes the assumption that spatial variations in gamma radiation intensity are locally smooth, which in turn permits approaching the problem of field estimation through the combination of multiple local regressions. This assumption, given sufficient sampling density, renders the method applicable in a variety of environments. With respect to the spectroscopy problem, this work further makes the assumption that sources of different isotopes are spatially distributed, reporting the isotope whose characteristic spectra dominates the set of measurements in a local area.

In reference to the notations listed in Table 1, the method spatially discretizes a bounded volume into a 3D grid $\mathbb{M}$ of cells with a resolution $\boldsymbol{D}_\mathbb{M} = [\boldsymbol{D}^x_\mathbb{M}, \boldsymbol{D}^y_\mathbb{M}, \boldsymbol{D}^z_\mathbb{M}]$. Each Counts Per Second (CPS) measurement ζ_κ acquired by the robot (at a fixed rate of 10 Hz) is pose-annotated using the robot's onboard odometry, and such pose-annotated measurements $\boldsymbol{\lambda}_\kappa = [\boldsymbol{\xi}_\kappa | \zeta_\kappa]$ are added to a list of readings maintained by the corresponding cell. Constructing this representation is essential for one of the algorithm's most critical functionalities, that of running gradient estimation, propagation, and spectral characterization at a rate independent of that of data collection.

Provided this underlying field representation, the proposed method for distributed gamma radiation field mapping consists of two stages, namely a) field estimation and b) field propagation. In the estimation stage, the set of spatially distributed readings are utilized over the discretized 3D grid $\mathbb{E}_\mathbb{M}$ in order to co-estimate the field's mean radiation intensity and an associated field gradient estimate. In the field propagation phase, the estimated gradient of each cell—in combination with a confidence metric based on the spatial entropy of the cell's neighboring measurements—is propagated to unknown neighboring cells using a weighted average. Subsequently, the measured and propagated gradients are used in order to propagate an estimated gamma radiation mean intensity for each cell. A visualization of the key steps of the method is provided in Figure 8.

Similarly, each spectral measurement, $\mathbf{Q}^\kappa$ is also pose-annotated using the robot's odometry, and is passed to a support vector machine (SVM) for classification. The SVM is

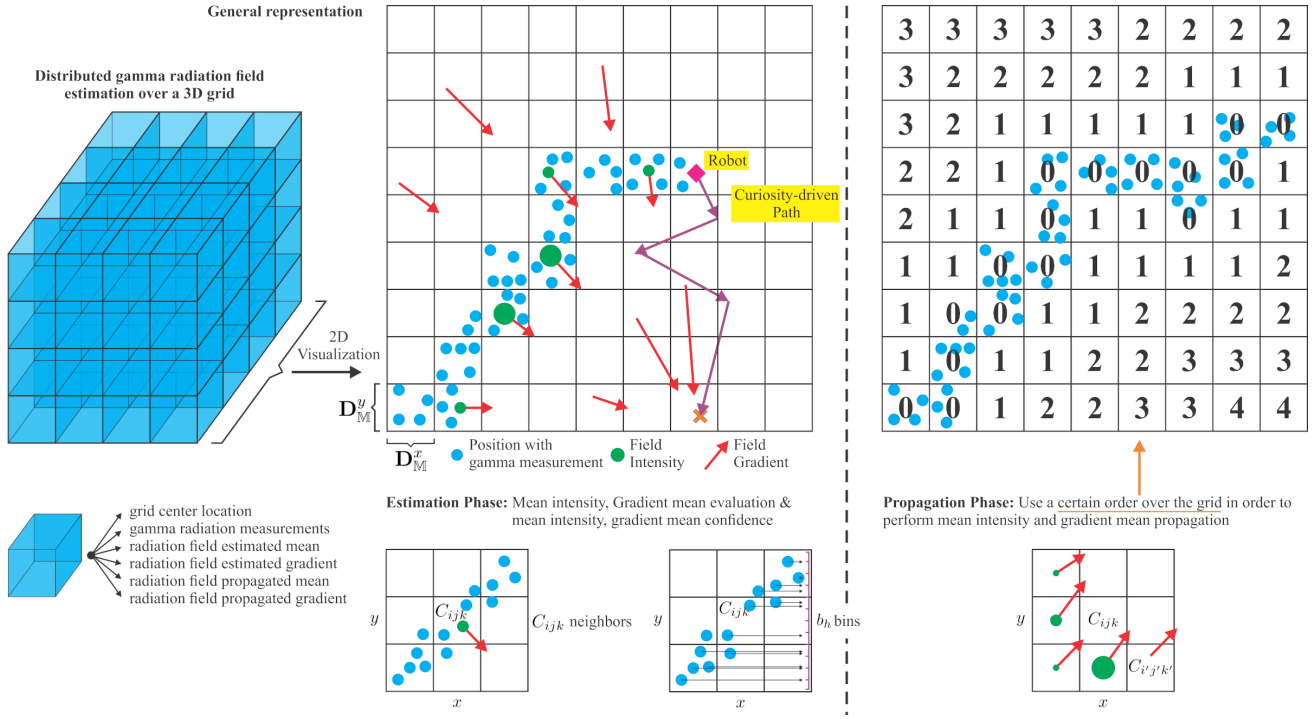

Fig. 8 Diagram depicting distributed radiation mapping technique. The blue cubes on the left depict how the environment is discretized into a grid of cells each containing a set of data members which track measured and propagated properties. The grid in the upper center shows a sparse representation of readings, estimated means, gradients and a curiosity driven path. The two grids in the lower center depict a group of neighboring cells deriving a gradient for the center, as well as it's entropy metric. Finally, the right side of the figure depicts how the propagation ordering is constructed as well as a set of neighbors contributing measured gradients to a neighbor of another layer.

trained using the characteristic spectra for a number of expected isotopes collected during calibration. In the experiments described in Section 6, the SVM is trained using the spectra shown in Figure 6. Given an accumulated unknown spectrum, the SVM derives the closest characteristic spectra using a linear kernel and a one vs. all evaluation strategy. The isotope with the strongest score is selected as the most likely isotope. This selection is treated as a vote for the chosen isotope, which is assigned to the corresponding cell, where each cell maintains a tally of all votes recorded within its bounds, denoted as $\mathbf{B}^m_{ijk}$.

4.1 Field Estimation

For a cell $\mathbb{C}_{ijk} \in \mathbb{M}$, we define its neighbors as the cells that share edges or faces with it. The radiation field gradient estimation step only considers measurements obtained within the neighborhood of a cell $\mathbb{C}_{ijk}$ (which includes the cell itself and its neighbors). Iterating over each of the cells in the map $\mathbb{C}_{ijk} \in \mathbb{M}$, the method first counts the number of readings N_{ijk} that are available inside a cell $\mathbb{C}_{ijk}$ in order to determine if it is sufficient in order to estimate the field mean intensity and gradient. If N_{ijk} is smaller than a set threshold N_{thres} then $\mathbb{C}_{ijk}$ is considered unmeasured. Otherwise, $\mathbb{C}_{ijk}$ is considered sufficiently sampled and the algorithm gathers all the readings in its neighborhood and runs a linear regression as in Eq. (6) to find the optimally fitting spatial gradient vector and mean:

$$\begin{bmatrix} \boldsymbol{\delta}^m_{ijk} \\ \mu^m_{ijk} \end{bmatrix} = (\mathbf{X}^T_{ijk}\mathbf{X}_{ijk})^{-1}\mathbf{X}^T_{ijk}\mathbf{S}_{ijk}. \tag{6}$$

These values are then assigned as the measured gradient vector of the cell $\boldsymbol{\delta}^m_{ijk}$ and measured mean intensity μ^m_{ijk}. In the event that the columns of the cell's measurement position matrix ($\mathbf{X}_{ijk}$) are not linearly independent, then the measured mean intensity is calculated as the average of the N^{nb}_{ijk} radiation readings in the neighborhood of cell $\mathbb{C}_{ijk}$. It is noted that this situation is rather rare due to the noise present in the onboard odometry estimates.

If the measured radiation intensity mean μ^m_{ijk} is smaller than a set threshold that reflects the background radiation level (μ^{bg}_{thres}), then $\boldsymbol{\delta}^m_{ijk}$ is assigned as $[0,0,0]^T$ in order to prevent gradients with very low Signal-to-Noise Ratio (SNR) from being erroneously propagated.

Finally, the algorithm derives confidence metrics for both the gradient $\boldsymbol{\delta}^m_{ijk}$ and mean intensity μ^m_{ijk} over each cell. The spatial entropy vector of the measurements acquired in the neighborhood of $\mathbb{C}_{ijk}$, $\mathbf{H}^m_{ijk}$, is derived and serves as a confidence metric for $\boldsymbol{\delta}^m_{ijk}$.

Table 1 Main notations used in this Section

$\mathbb{M}$	Discretized Grid Map
$i,j,k \in \mathbb{Z}^+$	Cell indexes along the x,y,z axes
$\mathbb{C}_{ijk}$	Grid cell at index i,j,k
$\mathbf{D}_{\mathbb{M}} \in \mathbb{R}^3$	Grid cell size in meters along x,y,z axes
$N_{ijk}, N^{nb}_{ijk} \in \mathbb{R}$	Number of measurements γ_m within $\mathbb{C}_{ijk}$ and $\mathbb{C}_{ijk}$'s neighborhood respectively
$\mathbf{X}_{ijk} \in \mathbb{R}^{n\times 4}$	Matrix of measurement positions within $\mathbb{C}_{ijk}$'s neighborhood, offset by the average measurement position, and appended with the column vector $\mathbf{1}$ at the end (the number of rows $n = N^{nb}_{ijk}$)
$\mathbf{S}_{ijk} \in \mathbb{R}^n$	Vector of intensity measurements within $\mathbb{C}_{ijk}$'s neighborhood (the number of rows $n = N^{nb}_{ijk}$)
$\mu^m_{ijk}, \sigma^m_{ijk} \in \mathbb{R}$	Estimated mean, mean confidence at $\mathbb{C}_{ijk}$
$\boldsymbol{\delta}^m_{ijk}, \mathbf{H}^m_{ijk} \in \mathbb{R}^3$	Vectors of estimated gradient, gradient confidence at $\mathbb{C}_{ijk}$
$\mathbb{O}^{\mu}$, $\mathbb{O}^{\delta}$	Cell propagation ordering for mean and gradient over $\mathbb{M}$
$\mu^p_{ijk}, \sigma^p_{ijk} \in \mathbb{R}$	Propagated mean, mean confidence at $\mathbb{C}_{ijk}$
$\boldsymbol{\delta}^p_{ijk}, \mathbf{H}^p_{ijk} \in \mathbb{R}^3$	Vectors of propagated gradient, gradient confidence at $\mathbb{C}_{ijk}$
$L^{\mu}_{ijk}, L^{\delta}_{ijk} \in \mathbb{Z}^+$	$\mathbb{C}_{ijk}$'s Propagation *Level*s for the mean and gradient vector
$\mathbf{Q}^{\kappa}_i$	The per-channel array of spectroscopic pulses recorded in channel i at time κ.
$\mathbf{G}^{\kappa}_i$	The raw count array of spectroscopic pulses recorded in channel i at time κ.
$\mathbf{B}^m_{ijk} \in \mathbb{R}^e$	Vector of measured spectral votes for each expected isotope recorded within $\mathbb{C}_{ijk}$(e is the number of expected isotopes)
$\mathbf{B}^p_{ijk} \in \mathbb{R}^e$	Vector of propagated spectral votes for each expected isotope recorded within $\mathbb{C}_{ijk}$(e is the number of expected isotopes)
$(\mathbf{a}^x, \mathbf{a}^y, \mathbf{a}^z)$	x,y,z components of vector $\mathbf{a} \in \mathbb{R}^3$

A histogram of measurement positions projected onto every axis of each cell is constructed employing b_h bins and is constrained by the limits of the neighborhood along each axis. Subsequently, Shannon Entropy is calculated based on this histogram as follows:

$$\mathbf{H}^{m,h}_{ijk} = -\sum_{w=1}^{b_h} P(h_w)\log P(h_w), \tag{7}$$
$$\mathbf{H}^{m}_{ijk} = [\mathbf{H}^{m,x}_{ijk}, \mathbf{H}^{m,y}_{ijk}, \mathbf{H}^{m,z}_{ijk}]^T,$$

where h_w represents the number of gamma radiation measurements along each axis h, $h \rightarrow x,y,x$, found in bin w. The term $P(h_w)$ is derived as follows:

$$P(h_w) = \frac{h_w}{\sum_{i=1}^{b_h} h_i}. \tag{8}$$

Regarding the confidence of the radiation field mean intensity associated with every cell's location, the following calculation takes place and reflects the number of measurements available locally:

$$\sigma^m_{ijk} = 1 - \frac{3}{N^{nb}_{ijk}},\ \sigma^m_{ijk} \in [0,1]. \tag{9}$$

The overall steps of the estimation phase used to derive the mean and gradients over the distributed field are summarized in Algorithm 1.

Algorithm 1 Measured Gradient Estimation

1: **for** $\mathbb{C}_{ijk} \in \mathbb{M}$ **do**
2: **if** $N_{ijk} > 4$ **then**
3: *Find neighbors of* $\mathbb{C}_{ijk}$
4: *Construct* $\mathbf{X}_{ijk}$ *and* $\mathbf{S}_{ijk}$
5: **if** $det(\mathbf{X}^T_{ijk}\mathbf{X}_{ijk}) != 0$ **then**
6: *Calculate* $\boldsymbol{\delta}^m_{ijk}$, μ^m_{ijk} *by Eq. (6)*
7: *Calculate* $\mathbf{H}^m_{ijk}$ *by Eq. (7)*, (8)
8: **else**
9: $\mu^m_{ijk} \leftarrow$ *Average*$(\mathbf{S}_{ijk})$
10: **end if**
11: *Calculate* σ^m_{ijk} *by Eq. (9)*
12: **if** $\mu^m_{ijk} <$ *background_threshold* μ^{bg}_{thres} **then**
13: $\boldsymbol{\delta}^m_{ijk} \leftarrow \mathbf{0}_{1\times 3}$
14: **end if**
15: **end if**
16: **end for**

Spectral characterization during the field estimation stage simply involves processing any cell which has at least one spectral vote in its corresponding $\mathbf{B}^m_{ijk}$, finding the isotope with the largest vote tally in it, and characterizing this cell as dominantly containing this isotope.

4.2 Field Propagation

The second essential component of the proposed distributed radiation field mapping methodology is that of mean and gradient propagation. This process is implemented using a carefully dictated cell ordering (Figure 8) that starts with cells whose means and gradients have been estimated using Algorithm 1 and continuing onto their neighbors. After the gradient estimation step is conducted, a cell has a valid mean as long as the condition set in line 2 of Algorithm 1 is satisfied, whereas a cell has a valid gradient vector if both conditions in lines 2, 5 of Algorithm 1 are satisfied. To produce the appropriate propagation orders for each cell, the proposed method defines separate propagation levels for the intensity mean (L^{μ}_{ijk}) and gradient vector (L^{δ}_{ijk}) using a recursive method. Specifically, the derivation of the level values for L^{μ}_{ijk} is detailed in Algorithm 2, while the derivation of L^{δ}_{ijk} is similar. Accordingly, distinct propagation orders $\mathbb{O}^{\mu}$, $\mathbb{O}^{\delta}$, are derived for the intensity mean propagation and gradient propagation processes provided the incremental ordering of L^{μ}_{ijk} and L^{δ}_{ijk}.

Algorithm 2 Cell Mean Level Derivation L^{μ}_{ijk}

NextLayer, CurrentLayer $\leftarrow \emptyset$ ▷ (Empty Set)
for $\mathbb{C}_{ijk} \in \mathbb{M}$ **do**
  $L^{\mu}_{ijk} \leftarrow NaN$
  if $N_{ijk} > 4$ **then**
    Add $\mathbb{C}_{ijk}$ *to CurrentLayer*
  end if
end for
$i \leftarrow 0$
while *CurrentLayer* $!= \emptyset$ **do**
  for $\mathbb{C}_{ijk} \in$ *CurrentLayer* **do**
    $L^{\mu}_{ijk} = i$
    for $\mathbb{C}_{i'j'k'} \in Neighbors(\mathbb{C}_{ijk})$ **do**
      if $L^{\mu}_{i'j'k'} = NaN$ **then**
        Add $\mathbb{C}_{i'j'k'}$ *to NextLayer*
      end if
    end for
  end for
  CurrentLayer $\leftarrow$ *NextLayer*
  NextLayer $\leftarrow \emptyset$
  $i \leftarrow i+1$
end while

Once the propagation ordering sequences have been derived then the field gradients are propagated first. For each grid cell $\mathbb{C}_{ijk}$ that is within the gradient propagation ordering $\mathbb{O}^{\delta}$, the method acquires its neighbors. For every cell with level $L^{\delta}_{ijk} = 0$, the cell's propagated gradient vector, $\boldsymbol{\delta}^{p}_{ijk}$, and gradient confidence vector, $\mathbf{H}^{p}_{ijk}$, are assigned to the corresponding estimates $\boldsymbol{\delta}^{m}_{ijk}$ and $\mathbf{H}^{m}_{ijk}$ of the cell, respectively. Otherwise, the cell's $\boldsymbol{\delta}^{p}_{ijk}$ is derived as the weighted average of the $\boldsymbol{\delta}^{p}_{ijk}$ values of its neighbors using only neighbors with L^{δ}_{ijk} less than that of the cell in question, and weighted by the neighbor's confidence metric $\mathbf{H}^{p}_{ijk}$.

Once gradient propagation is complete, mean propagation takes place as outlined in Algorithm 3. In particular, we iterate over cells in the mean propagation order, $\mathbb{O}^{\mu}$. For cells whose $L^{\mu}_{ijk} = 0$, their propagated mean (μ^{p}_{ijk}) and mean confidence (σ^{p}_{ijk}) are assigned to the corresponding estimated values μ^{m}_{ijk} and σ^{m}_{ijk} of the cell, respectively. For cells of all other levels, the method finds neighbors ($\mathbb{C}_{i'j'k'}$) of the cell whose $L^{\mu}_{i'j'k'}$ is less than that of the cell in question ($\mathbb{C}_{ijk}$), and calculates their corresponding contribution following the equations:

$$\mu^{p}_{i'j'k'\rightarrow ijk} = \mu^{p}_{i'j'k'} + \begin{bmatrix} (i-i')\mathbf{D}^{x}_{\mathbb{M}} \\ (j-j')\mathbf{D}^{y}_{\mathbb{M}} \\ (k-k')\mathbf{D}^{z}_{\mathbb{M}} \end{bmatrix}^{T} \boldsymbol{\delta}^{p}_{i'j'k'}, \tag{10}$$

$$\mathbf{D}_{M} = [\mathbf{D}^{x}_{\mathbb{M}}, \mathbf{D}^{y}_{\mathbb{M}}, \mathbf{D}^{z}_{\mathbb{M}}],$$

where $\mu^{p}_{i'j'k'\rightarrow ijk}$ is the contribution of the neighboring cell $\mathbb{C}_{i'j'k'}$ to the cell $\mathbb{C}_{ijk}$ ($L^{\mu}_{i'j'k'} < L^{\mu}_{ijk}$). The cell's μ^{p}_{ijk} is assigned as the average neighbor contribution ($\mu^{p}_{i'j'k'\rightarrow ijk}$) and weighted by the neighbor's $\sigma^{p}_{i'j'k'}$. The cell's σ^{p}_{ijk} is assigned as the average of the neighbors' $\sigma^{p}_{i'j'k'}$.

Algorithm 3 Mean Propagation
Given derived mean propagation ordering, $\mathbb{O}^{\mu}$

for $\mathbb{C}_{ijk} \in \mathbb{O}^{\mu}$ **do**
  if $L^{\mu}_{ijk} = 0$ **then**
    $\mu^{p}_{ijk}, \sigma^{p}_{ijk} = \mu^{m}_{ijk}, \sigma^{m}_{ijk}$
  else
    Contributions $\leftarrow \emptyset$ ▷ (Empty Set)
    Weights $\leftarrow \emptyset$
    for $\mathbb{C}_{i'j'k'} \in Neighbors(\mathbb{C}_{ijk})$ **do**
      if $L^{\mu}_{i'j'k'} < L^{\mu}_{ijk}$ **then**
        Calculate $\mu^{p}_{i'j'k'\rightarrow ijk}$ *by Eq. (10)*
        Add $\mu^{p}_{i'j'k'\rightarrow ijk}$ *to Contributions*
        Add $\sigma^{p}_{i'j'k'}$ *to Weights*
      end if
    end for
    $\mu^{p}_{ijk} \leftarrow$ *WeightedAverage(Contributions, Weights)*
    $\sigma^{p}_{ijk} \leftarrow$ *Average(Weights)*
  end if
end for

Within the propagation phase, the propagation of the estimated dominant isotopes throughout the map follows a process similar to that of mean propagation. The process follows the mean propagation ordering, $\mathbb{O}^{\mu}$. For each $\mathbb{C}_{ijk}$ whose L^{μ}_{ijk} is equal to 0, $\mathbb{C}_{ijk}$'s propagated spectral vote tally, $\mathbf{B}^{p}_{ijk}$ is assigned to that of its measured spectral vote tally, $\mathbf{B}^{m}_{ijk}$. Otherwise, the cell's $\mathbf{B}^{p}_{ijk}$ will be calculated as the sum of vote tallies of all of its neighbors belonging to a lower propagation level, L^{μ}_{ijk}. The cell then finds the isotope with the most votes, and is labelled with this isotope.

5 Next-Best-Radiation-Measurement Path Planning

Motivated by the above-described scenario, that of a small aerial robot entering a complex, GPS-denied, and geometrically confined environment in order to obtain a gamma radiation map of the environment, we address the problem of path planning seeking to guide the robot towards the next-best-radiation-measurement (NBRM) location.

Problem Definition The path planning problem described here faces two opposing constraints. First, given the limited endurance of aerial robots and the scale of the environments considered, an efficient path must be found that leads the robot to cover as much volume as possible, without wasting endurance in uninteresting, background radiation dominant areas of the environment. Second, and in opposition to the first, given the noise associated with gamma radiation measurements, the robot must obtain a) a sufficient number of measurements in locally contaminated areas to correctly estimate the mean, as well as b) sufficiently spatially distributed measurements to correctly estimate the gradient. To address these opposing factors, the planner (called "RadSniffer") is split into two components, a global planner responsible for leading the robot to the next most interesting

location, and a local planner designed to guarantee that the robot collects sufficient measurements that are appropriately spatially distributed. To promote the spatial distribution of measurements, the local planner introduces a metric based on the spatial entropy of the collected measurements. This metric is chosen given the assumption that more measurements with a greater spatial distribution provide more coverage and therefore a better sampling of the gradient to be estimated as described in Section 4.

To accomplish both planning tasks, the environment is spatially discretized into a grid of 3D cells, with a resolution $\mathbf{D}_P = [\mathbf{D}_P^x, \mathbf{D}_P^y, \mathbf{D}_P^z]$. This grid is completely separate from the grid used in the field estimation process and contains cells of larger dimension. While the grid cell size in the field estimation process dictates the resolution of the derived field intensity map, the grid cell size in the planning process discretizes the points of the map which the robot should visit to best characterize the map. The choice of planning grid resolution is therefore a balance between coverage and endurance, where a fine resolution will force the robot to visit a large number of cells, and a coarse resolution will cause the robot to execute long paths and will require more measurements to correctly classify a given cell. In the presented experiments, the mapping cells and planning cells are cuboids with edges of length 1 m and 2 m respectively.

The planner is updated at a frequency of 10 Hz. At each iteration, the planner first checks to see if the previously calculated path is complete. If so, the planner plans a new path depending on the state of the currently occupied planning cell. If the current path is not complete, the method will check for collisions on the current path. In the event the current path will cause a collision, the planner will stop the platform and plan a new path, in the same manner as in the case in which the current path has been completed. Figure 9 outlines the basic steps of the proposed planning strategy.

Table 2 Notations used in this Section

$\mathbb{M}_P$	Discretized Planning Grid Map
$i, j, k \in \mathbb{Z}^+$	Cell indexes along the x, y, z axes
$\mathbb{T}_{ijk}$	Planning grid cell at index i, j, k
$\mathbf{D}_P \in \mathbb{R}^3$	Planning grid cell size in meters along x, y, z axes
CDF_p	Background cumulative distribution function probability threshold
CDF_t	Background cumulative distribution function radiation threshold
b	Background radiation level
I_{mult}	Minimum background intensity multiplier
d_{min}	Minimum source intensity distance
$\mathbf{H}_{ijk}^{\hat{p}} \in \mathbb{R}^3$	Maximum possible planning entropy
$\mathbf{H}_{ijk}^{p} \in \mathbb{R}^3$	Planning cell entropy
$\mathbf{H}_{ijk}^{k} \in \mathbb{R}^3$	Planning cell entropy multiplier
$\mathbf{H}_{ijk}^{t} \in \mathbb{R}^3$	Planning cell entropy threshold

5.1 Statistical Testing

To plan a new path, the planner classifies cells into six independent states using three statistical tests: a background distribution test, a within range of background test, and an entropy test.

To determine whether or not a group of measurements belongs to the background distribution, a background test is employed using the Poisson Cumulative Distribution Function (CDF). The method constructs the CDF for a Poisson distribution whose mean is equal to the background level b, by:

$$CDF(x,b) = \sum_{i=0}^{x} \frac{e^{-b} b^i}{i!}. \tag{11}$$

Then, using a given probability threshold, CDF_p, the method calculates the mean radiation intensity level CDF_t below which will be considered to belong to the background distribution. If the mean of the readings present in a given planning cell is less than CDF_t, the cell is classified as belonging to background. Similarly the method uses Eq. (11) to calculate a number of measurements threshold N_{thresh}, using the given CDF_p, to classify background cells as measured or unmeasured.

In the interest of rapid exploration and to avoid wasting critical endurance in areas of background-dominant radiation, the method conducts a second test, the within range of background test. This test calculates a distance threshold, d_{min}, based on the inverse square law, by Eq. (12), and is a factor of the minimum intensity multiplier, I_{mult}, and the CDF_t calculated in Eq. (11). Any cell whose center is less than d_{min} from a background cell is considered within range of background. In short, the method assumes that no source greater than $b \times I_{mult}$ is within

$$d_{min} = \sqrt{\frac{b \times I_{mult}}{CDF_t}} \tag{12}$$

of any cell confirmed to be dominated by background. Finally, to determine whether or not the collected measurements within a given cell are sufficiently spatially distributed to accurately estimate a gradient, an entropy test is performed. The positions of readings within a planning cell are collected and their spatial entropy, $\mathbf{H}_{ijk}^{p}$ (where i, j, k correspond to the x, y, z axes respectively), is calculated using Eq. (7). The planner then calculates the maximum possible spatial entropy, $\mathbf{H}_{ijk}^{\hat{p}}$, within the cell. This calculation is performed by first sampling points within the cell which are collision free, and constructing a graph where edges connecting vertices are also collision free. Second, a connected components labeling procedure finds the subset of the free space samples which are connected to the current robot position. Eq. (7) is again calculated on this set of free space samples to render the theoretical maximum possible entropy, $\mathbf{H}_{ijk}^{\hat{p}}$. Finally, the test calculates an entropy threshold, $\mathbf{H}_{ijk}^{t}$ as the

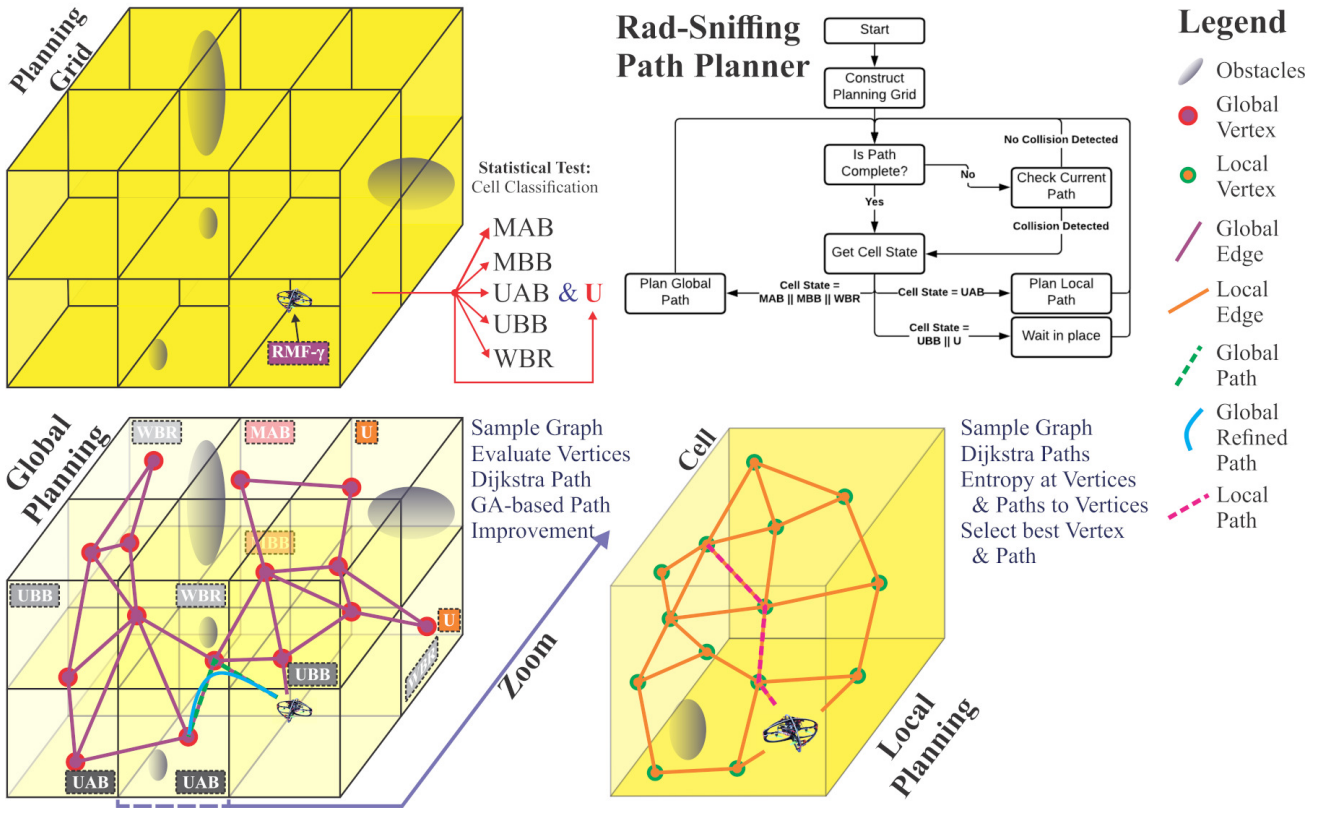

Fig. 9 Figure illustrating the "rad-sniffing" Next-Best-Radiation-Measurement (NBRM) planning process. A decision diagram is shown highlighting the various stages of the overall planning process, while drawings illustrate the discretization of the planning space, the process of global planning, as well as local planning within a single cell. The zoom component of the diagram highlights the process of local planning taking place within a single planing cell against the global planning process which takes place within a multitude of cells. The cell classification Unknown, or U, colored red, denotes that the current cell the robot is in, is Unknown.

element-wise product of a given multiplier, $\mathbf{H}^{k}_{ijk}$, and $\mathbf{H}^{\hat{p}}_{ijk}$, by Eq. (13):

$$\mathbf{H}^{t}_{ijk} = \mathbf{H}^{k}_{ijk} \odot \mathbf{H}^{\hat{p}}_{ijk}. \tag{13}$$

If any element of a cell's $\mathbf{H}^{p}_{ijk}$ is less than $\mathbf{H}^{t}_{ijk}$'s corresponding element, the cell is considered unmeasured.

5.2 Cell Classification

Using the above statistical tests, the proposed Next-Best-Radiation-Measurement (NBRM) planner classifies each of the cells into six independent states: Measured Above Background (MAB), Measured Below Background (MBB), Unmeasured Above Background (UAB), Unmeasured Below Background (UBB), Within Background Range (WBR), and Unknown (U). Cells whose $\mathbf{H}^{p}_{ijk}$ is above the entropy threshold, and whose measured mean is greater than the background threshold are classified as MAB. Cells which have more than N_{thresh} measurements whose measured mean is less than the background threshold are classified as MBB. Cells whose propagated mean is above the background threshold, but do not pass the spatial entropy test are classified as UAB. Cells whose propagated mean is below the background threshold but do not have more than N_{thresh} measurements are classified as UBB. Finally, any remaining cell is checked for proximity to a cell which is classified as MBB. Cells below the d_{min} threshold from such cells are marked as WRB, while remaining cells above d_{min} are marked as U.

Based on this cell classification, the NBRM planner decides which of the two distinct planning methods should be engaged. If the currently occupied cell's state is MAB, MBB, or WRB, the global planner will be initiated. If the currently occupied cell's state is UAB the local planner will be engaged. Finally, if the cell's state is UBB or U, the robot will wait at the current position until sufficient measurements have been collected to correctly classify the current cell. The planning behavior can be considered as follows: if the robot is currently within a cell which has not been sufficiently measured, as dictated by the tests described in Section 5.1, it will execute a local planning step to better characterize the current cell. Otherwise it will invoke the global planner to continue to explore the map and classify new cells.

5.3 Global Planning

The global planner mode seeks to lead the robot to more radiologically interesting parts of the map while avoiding areas which have already been mapped or have been determined to belong to the background areas of the environment. Global planning begins by building a planning graph. The planner first samples vertices in free space, and connects vertices with edges which are also collision-free. Second, the planner finds a destination cell by following a priority ordering of cells: UAB, UBB, WBR, U. Within each class, cells are sorted by their distance to the current position. The closest cell belonging to the highest priority class is selected. The planner then runs Dijkstra's Shortest Path Algorithm to find the shortest path from the current position to the free space sample closest to the center of destination cell.

5.3.1 Genetic Algorithm Path Improvement

Once again, given the aforementioned motivational scenario, the robot is expected to operate in confined spaces. The noise in the position estimate from the onboard odometry solution, coupled with the noisy depth estimates from the onboard mapping solution, as well as discretization errors which occur when building the TSDF map reveal real-world problems associated with simply choosing the shortest path between two points. For example, given a path which traverses a corner and sufficient free space sampling, Dijkstra's Shortest Path will find the path closest to the obstacle. This frequently causes collision detections as the robot follows the path given the noise sources described above.

To address this problem, global paths are augmented using a Genetic Algorithm (GA). The open source framework OpenGA [26] is used to optimize the derived path with respect to four fitness metrics: minimizing the average distance to a given target TSDF distance, minimizing the change in heading angle of the robot, minimizing the overall path length, and finally, minimizing the distance to a target z. This process returns short, straight paths, which attempt to maintain a given distance from obstacles, as well as a target height above the starting position. The implemented GA utilizes random point mutation, single point crossover, and Non-Dominated Sorting to iterate over generations to find a solution which optimizes the multi-objective problem. A genetic algorithm was chosen for three reasons: first, they are well suited to multi-objective problems, second, GA's follow simple rules making them intuitive to tune and utilize, and third, the described problem does not require the optimal solution, and therefore given endurance constraints, a GA based optimization process can be stopped after a given amount of time and is guaranteed to return a solution no worse than the initial solution. In this implementation the GA is limited to a total processing time of 500ms, and therefore consumes limited amount of the robot's overall endurance.

A GA is typically described by five operations: initialization, mutation, crossover, evaluation, and selection. The initialization operation generates a number of individuals to be inserted into the initial population by randomly mutating the initial path given by Dijkstra's Shortest Path. The mutation operation involves iterating through each point in the path. For each point, with a random probability, the GA will move the point by a random displacement vector. The crossover operation begins by randomly selecting two individuals, called parents, in the current population, then randomly selecting a point in each path. Two new individuals, called children, are generated by combining the vertices of the first parent between the starting vertex and the randomly selected vertex with the vertices of the second individual between the randomly selected vertex and last vertex. The other child is constructed with the remaining components of each parent. Evaluation takes place by calculating the fitness metrics for each path and sorting the individuals in the population using Non-Dominated Sorting. Non-Dominated sorting is a well described procedure [7], placing individuals in a number of pareto-optimal fronts. Finally, the selection procedure follows an elitist strategy selecting the members from the first pareto front, followed by the second front, up to the N^{th} front until a target number of individuals has been selected for the next generation. The GA procedure terminates when a maximum number of generations has been reached, or a stall count is exceeded indicating that there is marginal improvement between generations.

5.4 Local Planning

While the global planning mode seeks to maximize the global spread of the robot's trajectory, the local planning stage of the NBRM planner is engaged to ensure that the robot collects a sufficient number of measurements with sufficient spatial distribution in areas of strong radioactivity. From a high level, the local planner strives to find the location within the current cell which will maximize the planning cell's sampling entropy if the robot were to navigate to that point. To accomplish this objective, the local planner starts by randomly sampling free space points within the bounds of the current cell, and constructs a graph from these samples, connecting vertices with edges which are collision free. The planner then performs a brute force search of all of the collected samples. For each sample, the planner calculates the entropy of the set of points including the current measurement points, as well as points on the Dijkstra's Shortest Path from the current position to the sampled point. The best sampled point is the point which yields an anticipated entropy greater than the entropy threshold calculated in Eq. (13), on all three axes. The robot is then commanded to follow the Dijkstra's Shortest Path to this point.

Exp. #	# Sources	Radiation Mapping Cell Size (m) $\mathbf{D}_M^x \times \mathbf{D}_M^y \times \mathbf{D}_M^z$	Radiation Planning Cell Size (m) $\mathbf{D}_P^x \times \mathbf{D}_P^y \times \mathbf{D}_P^z$	Background Radiation Level (CPS) b	Entropy Multiplier $\mathbb{H}_{ijk}^k$	CDF Threshold CDF_p	Minimum Background Intensity Multiplier I_{mult}
1	9	1.0x1.0x1.0	2.0x2.0x2.0	6	0.45	0.95	1.5
2	2	1.0x1.0x1.0	2.0x2.0x2.0	12	0.45	0.95	2.5
3	8	1.0x1.0x1.0	2.0x2.0x2.0	12	0.45	0.95	2.5

Table 3 Table describing the configuration employed for each of the presented experiments.

6 Evaluation Studies

To evaluate the proposed system, including the platform (RMF-γ), the RadMapper radiation mapping and spectropic analysis framework, and the RadSniffer planning method, a set of real-world experiments are presented. In each experiment, the environment is completely unknown. The robot constructs its volumetric map of the environment in real time on board the robot in parallel with the radiation mapping, spectroscopy and planning framework presented in this work.

6.1 Experimental Evaluation

Three experiments were conducted to evaluate the system as a whole under real-world conditions. First, several radiation sources were placed in a machine shop environment. These radiation sources consisted of uranium tailings collected from an abandoned uranium mine outside of Reno, NV. The tailings are placed in several plastic containers isolated in two groups with a region of background between them. RMF-γ conducted a flight lasting approximately 5 min, successfully isolating and estimating both radiation sources. Figure 10 depicts the mission in several stages showing the progression of the exploration process, as well as the constructed voxel map of the occupied parts of the environment colored by the nearest cell's propagated mean. A linear color scale is applied where green indicates areas dominated by background radiation determined to be 6 CPS, and red indicating areas whose propagated mean exceeds 45 CPS.

The second and third experiments took place within a laboratory environment containing numerous sources of radiation. Specifically, in the second experiment (Radiation Lab #1), a ^{226}Ra source, measuring approximately 550 μRem/hr at a distance of 1 m, is placed at the location indicated by the letter B in Figure 12. A set of assorted, partially shielded sources, including primarily ^{226}Ra, but also including ^{137}Cs and ^{232}Th, measuring approximately 310 μRem/hr at a distance of 1 m, are present in a cabinet located at the point indicated by the letter A in Figure 12. In a single flight lasting approximately 5 min, RMF-γ successfully derives a radiation map of the contaminated environment. In the third experiment (Radiation Lab #2), a number of sources are placed throughout the environment indicated by labels A, B, C, D, E, F, G, and H in Figure 13. The previously described strong ^{226}Ra source is placed at the location indicated by the label B, containers of raw uranium ore are placed at the positions indicated by labels C and D. Finally, several assorted low intensity sources, primarily ^{226}Ra, but also including ^{137}Cs and ^{232}Th, are placed at the locations indicated by A, E, F, G, and H. Again, in a single flight lasting 5.5 min, RMF-γ successfully derives a map of the radiation field present in the environment. Table 5.4 details the environmental conditions, as well as the settings employed for the mapping and planning components.

Figure 11 depicts the spectral mapping results for the three experiments. The first experiment in the machine shop is the most successful, clearly identifying the sources correctly as ^{238}U. The second experiment, Radiation Lab #1, shows that the environment is dominated by ^{226}Ra, with false detections of ^{238}U, ^{137}Cs and ^{232}Th in areas of weak fields, especially at the borders of regions dominated by background. The third experiment, Radiation Lab #2, shows that the environment is dominated by both ^{238}U and ^{226}Ra, as well as false detections of ^{232}Th, similarly in regions with intensities near background.

7 Conclusions

This paper contributes a complete method for autonomous distributed gamma radiation field characterization through the combination of a field estimation and spectroscopy algorithm and an informative path planning strategy. The approach enables efficient estimation of the distributed radioactivity within complex and confined environments, alongside spectroscopic analysis identifying the radioisotope dominating each region of the map, using small aerial robots respecting their limited endurance capabilities. A prototype realization is then demonstrated using a tailor-made micro flying robot called RMF-γ which integrates a scintillator and photomultiplier combination enabling accurate radiological measurements at a small form factor. The overall technique is evaluated through a set of experimental studies involving the autonomous surveying, radiation mapping and characterization of narrow GPS-denied environments involving diverse real nuclear radioactive sources.

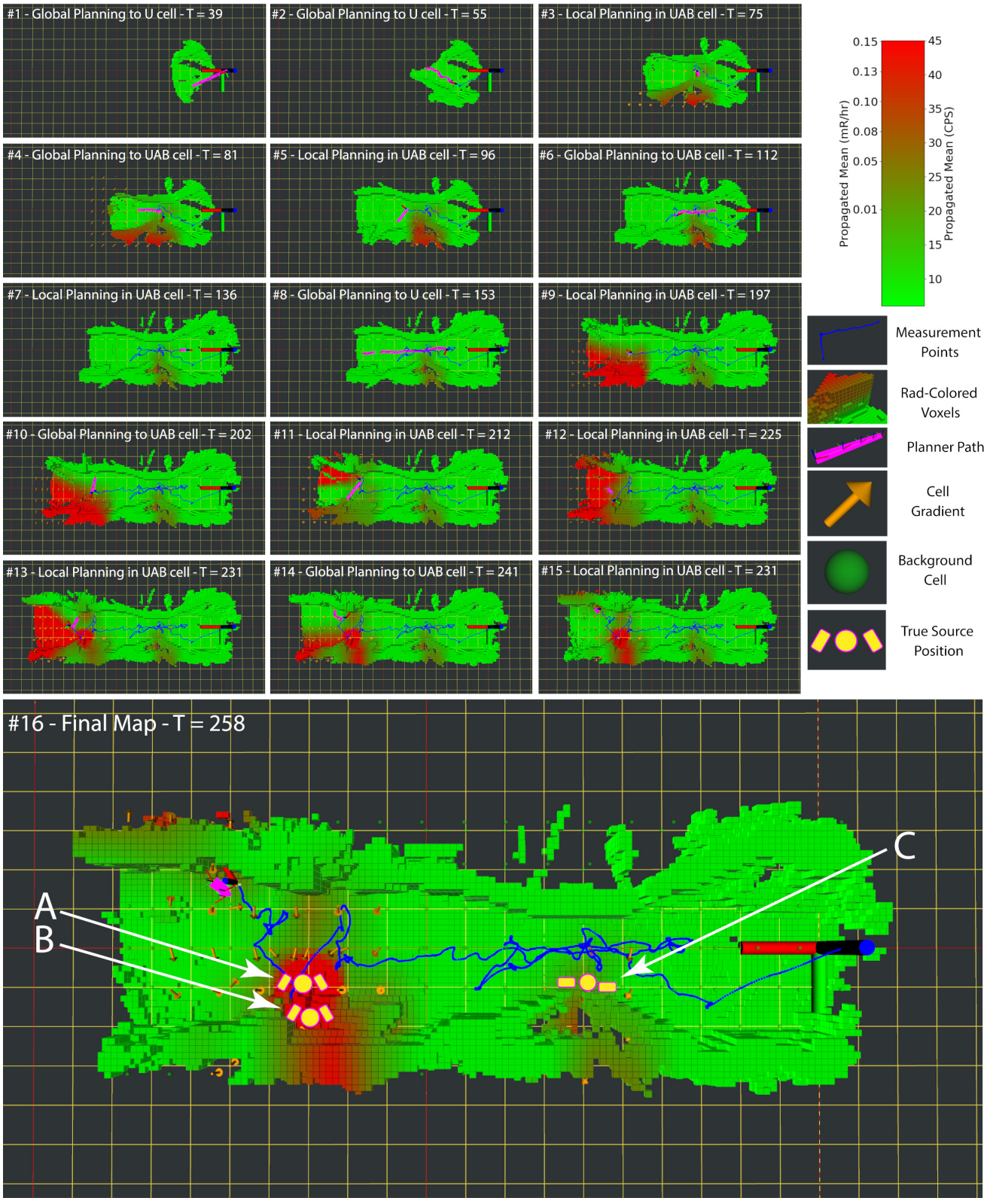

Fig. 10 A figure depicting an experiment within a machine-shop environment. Three buckets of uranium ore are placed in the environment at the locations indicated by A,B,C in the bottom map. The buckets are further supplemented by small boxes of uranium ore as depicted in the map. The upper portion of the figure depicts the 15 individual planning steps performed by RMF-γ platform while mapping the environment. In each step the occupied voxels of the environment are colored by their propagated field intensity. The blue lines indicate the positions of the pose annotated measurements, the orange arrows depict the propagated radiation gradient, and the pink line depicts the path calculated at that iteration. As shown in planning step #3, the first cell above the background radiation level is found after planning step #2, 55 seconds into the mission, at which point the local planner is engaged to estimate the radiation field map in this cell. This local planning step yields a new cell which has been labeled as Unknown Above Background (UAB) to which RMF-γ plans a new path towards in planning step #4. This source, at location C, has been identified and mapped after planning step #7, and therefore the robot continues its exploration deeper into the unknown parts of the map by engaging the global planner in planning step #8. This process continues until planning step #15 at which point the system's battery is depleted and RMF-γ is forced to land.

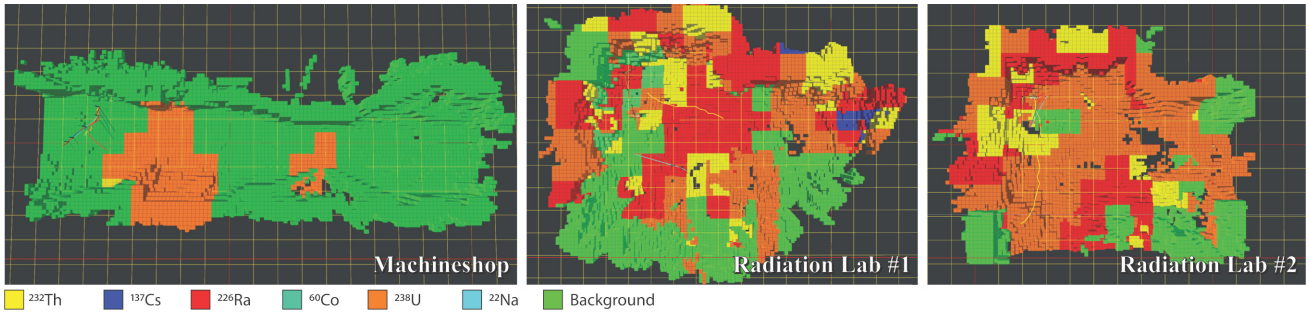

Fig. 11 Figure depicting the spectral characterization obtained at the end of each of the three experiments presented. *Machine shop:* The vast majority of the environment is classified as background, while the two uranium source positions are correctly identified as uranium. *Radiation Lab #1:* The environment is dominated by radium. Several false detections of uranium, thorium and cesium are also found in areas of weak intensity and in areas bordering regions of background radiation. *Radiation Lab #2:* The environment is dominated by radium and uranium, reflecting the strongest sources present. False detections of thorium are found in few locations due to the fact that the planner does not plan local paths for the purposes of identifying isotopes and the combination of a large number of different isotopes as present in this environment may lead to incorrect classification without a significant number of samples.

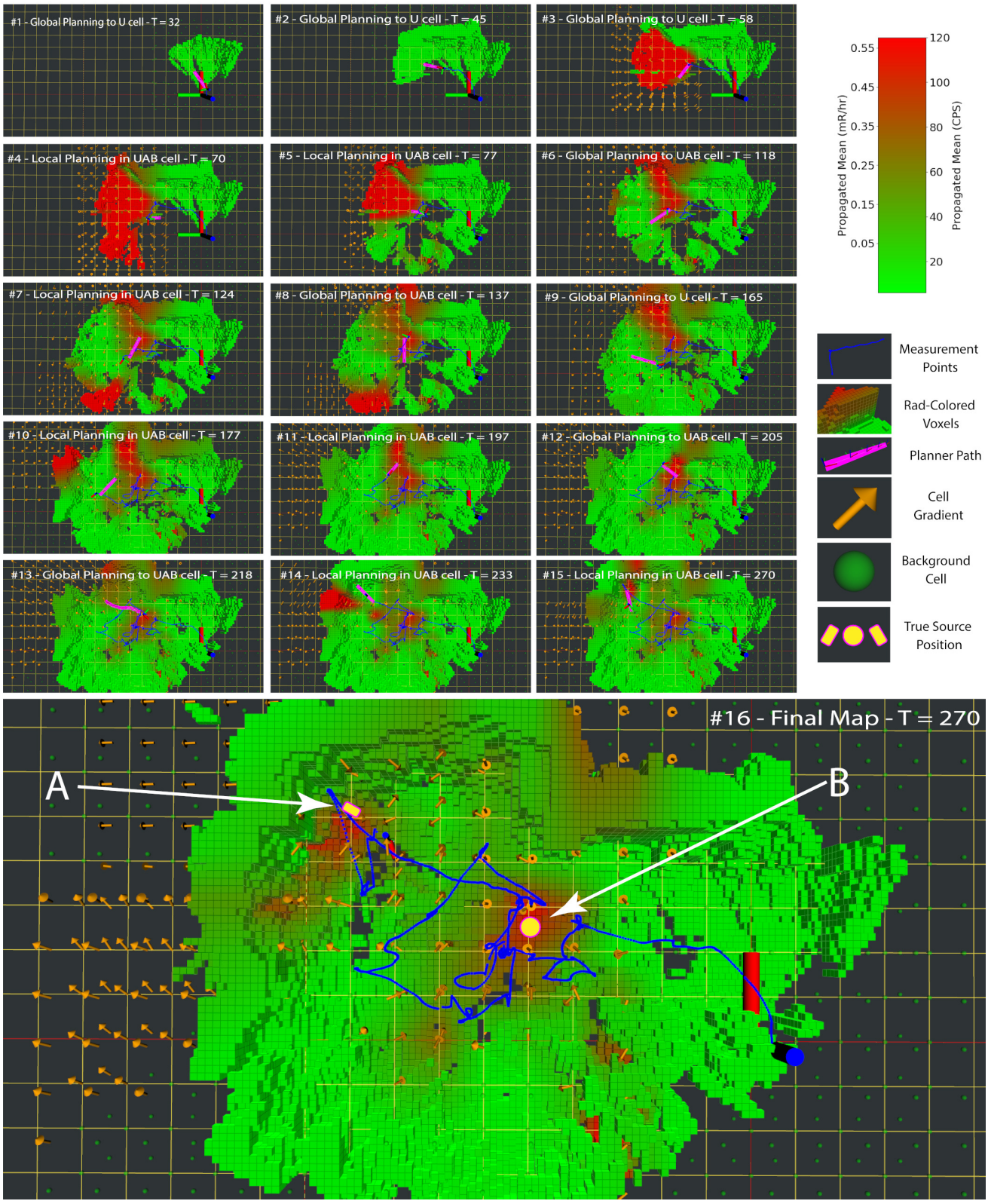

Fig. 12 A figure depicting the first of two experiments performed within a laboratory environment. A very strong radium source is placed at the location indicated by B in the lower map, while a partially shielded set of assorted sources is stored in a cabinet at the position indicated by A. The maps above depict 15 of the planning steps executed while conducting the mapping mission. The orange arrows indicate the propagated radiation gradient, while the occupied voxels are colored by the propagated mean of the nearest mapping cell.

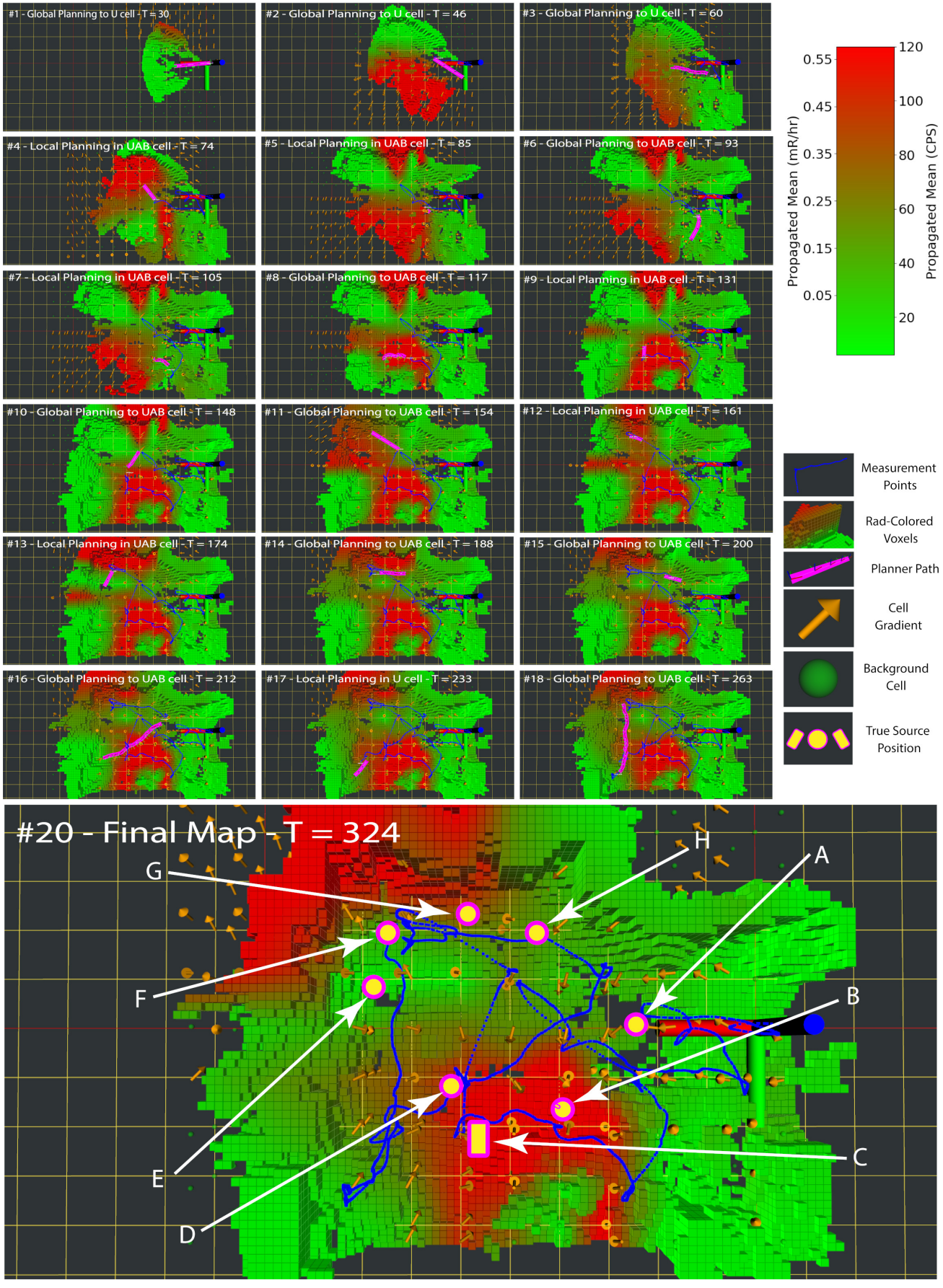

Fig. 13 A figure depicting the second of two experiments performed within a laboratory environment. In this experiment a number of sources are distributed throughout the environment with variable intensities indicated by the labels A,B,C,D,E,F,G, and H. The maps above depict 18 of the planning steps executed while conducting the mapping mission. The orange arrows indicate the propagated radiation gradient, while the occupied voxels are colored by the propagated mean of the nearest mapping cell.

References

1. Baca, T., Stibinger, P., Doubravova, D., Turecek, D., Solc, J., Rusnak, J., Saska, M., Jakubek, J.: Gamma radiation source localization for micro aerial vehicles with a miniature single-detector compton event camera. In: International Conference on Unmanned Aircraft Systems (ICUAS). IEEE (2021)
2. Baidoo-Williams, H.E.: Maximum likelihood localization of radiation sources with unknown source intensity. arXiv preprint arXiv:1608.00427 (2016)
3. Baidoo-Williams, H.E., Mudumbai, R., Bai, E., Dasgupta, S.: Some theoretical limits on nuclear source localization and tracking. In: Information Theory and Applications Workshop (ITA), 2015, pp. 270–274. IEEE (2015)
4. Christie, G., Shoemaker, A., Kochersberger, K., Tokekar, P., McLean, L., Leonessa, A.: Radiation search operations using scene understanding with autonomous uav and ugv. Journal of Field Robotics (2016)
5. Cordone, G., Brooks, R.R., Sen, S., Rao, N.S., Wu, C.Q., Berry, M.L., Grieme, K.M.: Improved multi-resolution method for mle-based localization of radiation sources. In: Information Fusion (Fusion), 2017 20th International Conference on, pp. 1–8. IEEE (2017)
6. Cortez, R.A., Tanner, H.G., Lumia, R.: Distributed robotic radiation mapping. In: Experimental Robotics, pp. 147–156. Springer (2009)
7. Deb, K., Agrawal, S., Pratap, A., Meyarivan, T.: A fast elitist non-dominated sorting genetic algorithm for multi-objective optimization: Nsga-ii. In: International conference on parallel problem solving from nature, pp. 849–858. Springer (2000)
8. F. Mascarich, T. Wilson, C. Papachristos, and K. Alexis: Radiation source localization in gps-denied environments using aerial robots. In: IEEE International Conference on Robotics and Automation (ICRA) (2018)
9. Feldman, G.J., Cousins, R.D.: Unified approach to the classical statistical analysis of small signals. Physical Review D **57**(7), 3873 (1998)
10. Fetter, S., Cochran, T.B., Grodzins, L., Lynch, H.L., Zucker, M.S.: Gamma-ray measurements of a soviet cruise-missile warhead. Science **248**(4957), 828–834 (1990)
11. Gabrlik, P., Lazna, T., Jilek, T., Sladek, P., Zalud, L.: An automated heterogeneous robotic system for radiation surveys: Design and field testing. Journal of Field Robotics
12. Groves, K., Hernandez, E., West, A., Wright, T., Lennox, B.: Robotic exploration of an unknown nuclear environment using radiation informed autonomous navigation. Robotics **10**(2), 78 (2021)
13. Guzman, R., Navarro, R., Ferre, J., Moreno, M.: Rescuer: Development of a modular chemical, biological, radiological, and nuclear robot for intervention, sampling, and situation awareness. Journal of Field Robotics **33**(7), 931–945 (2016)
14. Jarman, K.D., Miller, E.A., Wittman, R.S., Gesh, C.J.: Bayesian radiation source localization. Nuclear technology **175**(1), 326–334 (2011)
15. Jones, H., Maley, S., Yonekawa, K., Mousaei, M., Yesso, J.D., Kohanbash, D., Whittaker, W.: Automated analysis, reporting, and archiving for robotic nondestructive assay of holdup deposits. arXiv preprint arXiv:1901.10795 (2019)
16. Kazemeini, M., Cook, Z., Lee, J., Barzilov, A., Yim, W.: Plug-and-play radiation sensor components for unmanned aerial system platform. Journal of Radioanalytical and Nuclear Chemistry **318**(3), 1797–1803 (2018)
17. Knoll, G.F.: Radiation detection and measurement. John Wiley & Sons (2010)
18. La, H.M., Sheng, W.: Distributed sensor fusion for scalar field mapping using mobile sensor networks. IEEE Transactions on cybernetics **43**(2), 766–778 (2013)
19. M. Jacoby: As nuclear waste piles up, scientists seek the best long-term storage solutions. URL `https://cen.acs.org/environment/pollution/nuclear-waste-pilesscientists-seek-best/98/i12`. Online; accessed 12 July 2021
20. Maimone, M., Matthies, L., Osborn, J., Rollins, E., Teza, J., Thayer, S.: A photo-realistic 3-d mapping system for extreme nuclear environments: Chernobyl. In: Intelligent Robots and Systems, 1998. Proceedings., 1998 IEEE/RSJ International Conference on, vol. 3, pp. 1521–1527. IEEE (1998)
21. Martínez, S.: Distributed interpolation schemes for field estimation by mobile sensor networks. IEEE Transactions on Control Systems Technology **18**(2), 491–500 (2010)
22. Mascarich, F., De Petris, P., Nguyen, H., Alexis, K.: Autonomous distributed 3d radiation field estimation for nuclear environment characterization. In: 2021 IEEE International Conference on Robotics and Automation (ICRA). IEEE (2021)
23. Mascarich, F., Papachristos, C., Wilson, T., Alexis, K.: Distributed radiation field estimation and informative path planning for nuclear environment characterization. In: 2019 International Conference on Robotics and Automation (ICRA), pp. 2318–2324. IEEE (2019)
24. Mayhew, C.G., Sanfelice, R.G., Teel, A.R.: Robust source-seeking hybrid controllers for autonomous vehicles. In: American Control Conference, 2007. ACC'07, pp. 1185–1190. IEEE (2007)
25. Mazumdar, A., Lozano, M., Fittery, A., Asada, H.H.: A compact, maneuverable, underwater robot for direct inspection of nuclear power piping systems. In: Robotics and Automation (ICRA), 2012 IEEE International Conference on, pp. 2818–2823. IEEE (2012)
26. Mohammadi, A., Asadi, H., Mohamed, S., Nelson, K., Nahavandi, S.: Openga, a c++ genetic algorithm library. In: Systems, Man, and Cybernetics (SMC), 2017 IEEE International Conference on, pp. 2051–2056. IEEE (2017)
27. Newaz, A.A.R., Jeong, S., Lee, H., Ryu, H., Chong, N.Y.: Uav-based multiple source localization and contour mapping of radiation fields. Robotics and Autonomous Systems **85**, 12–25 (2016)
28. Newaz, A.A.R., Jeong, S., Lee, H., Ryu, H., Chong, N.Y., Mason, M.T.: Fast radiation mapping and multiple source localization using topographic contour map and incremental density estimation. In: Robotics and Automation (ICRA), 2016 IEEE International Conference on, pp. 1515–1521. IEEE (2016)
29. Oleynikova, H., Taylor, Z., Fehr, M., Siegwart, R., Nieto, J.: Voxblox: Incremental 3d euclidean signed distance fields for on-board mav planning. In: 2017 IEEE/RSJ International Conference on Intelligent Robots and Systems (IROS), pp. 1366–1373. IEEE (2017)
30. Pang, S., Farrell, J.A.: Chemical plume source localization. IEEE Transactions on Systems, Man, and Cybernetics, Part B (Cybernetics) **36**(5), 1068–1080 (2006)
31. Rolf, E., Fridovich-Keil, D., Simchowitz, M., Recht, B., Tomlin, C.: A successive-elimination approach to adaptive robotic source seeking. IEEE Transactions on Robotics (2020)
32. Sato, Y., Terasaka, Y., Utsugi, W., Kikuchi, H., Kiyooka, H., Torii, T.: Radiation imaging using a compact compton camera mounted on a crawler robot inside reactor buildings of fukushima daiichi nuclear power station. Journal of Nuclear Science and Technology **56**(9-10), 801–808 (2019)
33. Štibinger, P., Báča, T., Saska, M.: Localization of ionizing radiation sources by cooperating micro aerial vehicles with pixel detectors in real-time. IEEE Robotics and Automation Letters **5**(2), 3634–3641 (2020)
34. Towler, J., Krawiec, B., Kochersberger, K.: Radiation mapping in post-disaster environments using an autonomous helicopter. Remote Sensing **4**(7), 1995–2015 (2012)
35. Vetter, K., Chivers, D., Quiter, B.: Advanced concepts in multi-dimensional radiation detection and imaging. In: Nuclear Threats and Security Challenges, pp. 179–192. Springer (2015)

36. Wan, H., Zhang, T., Zhu, Y.: Detection and localization of hidden radioactive sources with spatial statistical method. Annals of Operations Research **192**(1), 87–104 (2012)
37. Wang, Y., Ishwar, P.: Distributed field estimation with randomly deployed, noisy, binary sensors. IEEE Transactions on Signal Processing **57**(3), 1177–1189 (2009)
38. World Nuclear Association: Decommissioning Nuclear Facilities. URL https://www.world-nuclear.org/information-library/nuclear-fuel-cycle/nuclear-wastes/decommissioning-nuclear-facilities.aspx. Online; accessed 16 July 2021
39. World Nuclear Association: Storage and Disposal of Radioactive Waste. URL https://world-nuclear.org/information-library/nuclear-fuel-cycle/nuclear-waste/storage-and-disposal-of-radioactive-waste.aspx. Online; accessed 23 July 2021
40. Zhang, C., Arnold, D., Ghods, N., Siranosian, A., Krstic, M.: Source seeking with non-holonomic unicycle without position measurement and with tuning of forward velocity. Systems & control letters **56**(3), 245–252 (2007)